

# Production of hadronic resonances measured with ALICE at the LHC

**Jihye Song (for the ALICE Collaboration)**

Department of Physics, University of Houston, Houston, Texas, USA

E-mail: [Jihye.Song@cern.ch](mailto:Jihye.Song@cern.ch)

**Abstract.** Measurements of short-lived hadronic resonances are used to probe the properties of the hadronic phase in ultra-relativistic heavy-ion collisions. Since these resonances have lifetimes comparable to that of the produced fireball, they are sensitive to the competitive rescattering and regeneration effects in the hadronic gas, which modify the observed particle momentum distributions and yields after hadronization. Having different masses, quantum numbers, and quark content, hadronic resonances can provide insight into processes that determine the shapes of particle momentum spectra, strangeness production, and the possible onset of collective effects in small systems.

We here present the latest results on  $\rho(770)^0$ ,  $K^*(892)$ ,  $\phi(1020)$ ,  $\Sigma(1385)^\pm$ ,  $\Lambda(1520)$ ,  $\Xi(1530)^0$  and  $\Xi(1820)$  production in pp, p–Pb, Pb–Pb and Xe–Xe collisions at different LHC energies. Results include system-size and collision-energy evolution of transverse momentum spectra, integrated yields, mean transverse momenta, particle ratios, and nuclear modification factors.

## 1. Introduction

Hadronic resonances with various lifetimes are valuable probes to study the properties of the hadronic medium formed in ultra-relativistic heavy-ion collisions, since the yield ratios of resonances to stable hadrons provide information about the re-scattering and regeneration effects in the hadronic medium. If the loss of resonances due to elastic or pseudo-elastic scattering of their decay products (re-scattering) is dominant over regeneration, the resonance yield after kinetic freeze-out will be smaller than the one originally produced at the chemical freeze out. Considering the expected lifetime of the hadronic phase ( $\sim 10$  fm/c), the measurement of the production of a comprehensive set of resonances with different lifetimes can be used to study the interplay of particle re-scattering and regeneration.

Studies of strangeness production play an important role in understanding the matter produced in heavy-ion collisions. Measurements of strange and non-strange particle yields can be described by grand-canonical thermal models in heavy-ion collisions [1], while canonical suppression is expected in small systems [2, 3]. Enhancement of strangeness production has been observed in high energy nucleus–nucleus (A–A) collisions with respect to pp collisions at RHIC (Relativistic Heavy-Ion Collider) and LHC (Large Hadron Collider) energies [4]. The study of strangeness production as a function of the charged particle multiplicity produced in the collision systems from pp to A–A, therefore, allows one to investigate the origin of the enhancement.



Particles with open strangeness may be subject to canonical suppression in small collision systems with respect to large systems, whereas the  $\phi$ , a particle with hidden strangeness, is not expected to be canonically suppressed. Comparisons of particles with open and hidden strangeness can help to understand strangeness production.

## 2. Experiment

The ALICE experiment [5] is particularly well suited to study the production of both identified and unidentified charged particles thanks to its excellent tracking performance coupled with extensive particle identification (PID) capabilities over a wide range of transverse momentum. In the central barrel, the Inner Tracking System (ITS) and the Time Projection Chamber (TPC) are used for charged-particle tracking and primary collision vertex reconstruction. The ITS consists of three sub-detectors of two layers each, covering a central pseudorapidity range  $|\eta| < 0.9$ : Silicon Pixel Detector (SPD), Silicon Drift Detector (SDD) and Silicon Strip Detector (SSD). The TPC is the main charged particle tracking detector, and has full azimuthal coverage in the pseudorapidity range  $|\eta| < 0.9$ . Along with track reconstruction, it also provides a measurement of the momentum and excellent particle identification. The TPC provides the measured specific energy loss ( $dE/dx$ ) to identify the particles, especially in low momentum range ( $p < 1$  GeV/c) where the  $dE/dx$  of particles are well separated. To extend the particle identification to higher  $p_T$ , the Time of Flight (TOF) detector is used in addition to the TPC information. It covers a pseudorapidity range  $|\eta| < 0.9$  and provides excellent PID capabilities in the intermediate  $p_T$  range by exploiting the time-of-flight information. The forward V0 detector, a scintillator detector with a timing resolution less than 1 ns, is used for centrality selection, triggering and beam-induced background rejection. The V0 consists of two sub-detectors, V0A and V0C, placed at asymmetric positions, one on each side of the interaction point with full azimuthal acceptance and cover the pseudorapidity ranges  $2.8 < \eta < 5.1$  and  $-3.7 < \eta < -1.7$ , respectively. The year and different collision energies for accumulated data in different collision systems are summarized in Table 1. The list of resonances that we report is provided in Table 2 with their quark content, decay modes exploited for the measurements, and branching ratios.

**Table 1.** Year for accumulated data sample and center of mass energy for different collision systems.

	Pb–Pb	Xe–Xe	p–Pb	pp
Year	2010-2011, 2015, 2018	2017	2013, 2016	2009-2013, 2015-2018
$\sqrt{s_{NN}}$ [TeV]	2.76, 5.02	5.44	5.02, 8.16	0.9, 2.76, 7, 8, 5.02, 13

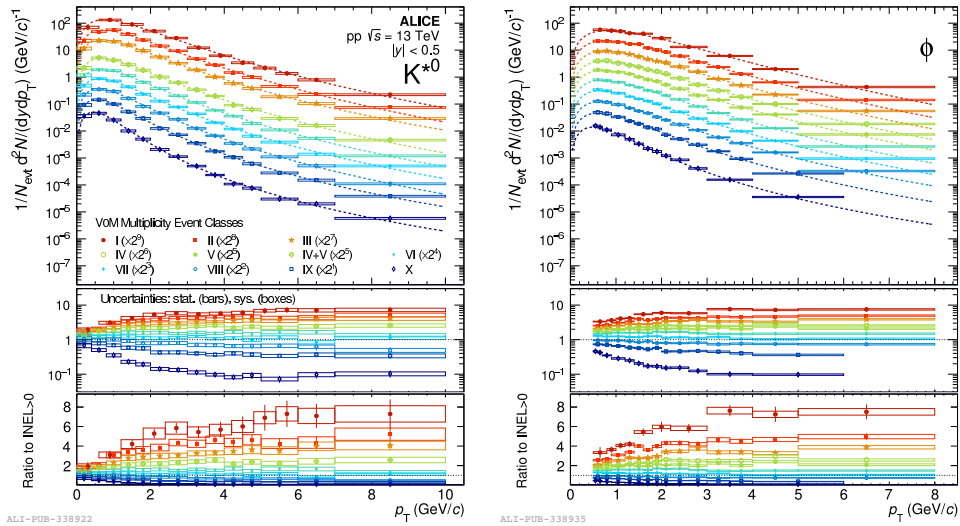
## 3. Results and discussion

### 3.1. Transverse momentum spectra

The  $p_T$  spectra for  $K^{*0}$  and  $\phi$  in the various multiplicity classes in pp collisions at  $\sqrt{s} = 13$  TeV are shown in Figure 1 with the ratios of these spectra to the inclusive INEL>0 spectrum [7]. Note that, the INEL>0 event class is defined as the set of inelastic collisions with at least one charged particle in the range  $|\eta| < 1$ . For  $p_T \leq 5$  GeV/c the evolution of spectral shape from low to high multiplicity has been observed. For higher  $p_T$ , the spectra in different multiplicity classes all have similar shape, indicating that the processes that change the shape of the  $p_T$  spectra in different multiplicity classes are dominant at low  $p_T$ .

**Table 2.** Lifetime of the measured resonances with their quark content, decay modes exploited for the measurements presented here and branching ratios [6].

	$c\tau$ (fm)	quark content	Decay modes	BR [%]
$\rho(770)^0$	1.3	$(u\bar{u}+d\bar{d})/\sqrt{2}$	$\pi^+\pi^-$	100
$K^*(892)^0$	4.2	$d\bar{s}$	$K^+\pi^-$	66.6
$\Sigma(1385)^+$	5.5	$uus$	$\Lambda\pi^+ \rightarrow (p\pi^-)\pi^+$	87.0
$\Sigma(1385)^-$	5.0	$dds$	$\Lambda\pi^- \rightarrow (p\pi^-)\pi^-$	87.0
$\Xi(1820)^-$	8.1	$dss$	$\Lambda K \rightarrow (p\pi^-)K$	unknown
$\Lambda(1520)$	12.6	$uds$	$p + K^-$	22.5
$\Xi(1530)^0$	21.7	$uss$	$\Xi^-\pi^+ \rightarrow (\Lambda\pi^-)\pi^+ \rightarrow ((p\pi^-)\pi^-)\pi^+$	66.7
$\phi(1020)^0$	44	$s\bar{s}$	$K^+K^-$	48.9

**Figure 1.**  $p_T$  spectra of  $K^{*0}$  and  $\phi$  in pp collisions at  $\sqrt{s} = 13$  TeV for different multiplicity classes, scaled by factors as indicated [7]. The lower panels show the ratios of the multiplicity-dependent  $p_T$  spectra to the multiplicity-integrated INEL>0 spectra (with both linear and logarithmic vertical scales)

### 3.2. $p_T$ integrated yields $dN/dy$ and resonance particle ratios

The  $p_T$ -integrated yields  $dN/dy$  of  $K^{*0}$  and  $\phi$  are extracted from the  $p_T$  spectra in different multiplicity classes and presented in Figure 2 as functions of  $\langle dN_{ch}/d\eta_{lab} \rangle_{|\eta|<0.5}$ . For both particles,  $dN/dy$  exhibits an approximately linear increase with increasing  $\langle dN_{ch}/d\eta_{lab} \rangle_{|\eta|<0.5}$ . Results for pp collisions at  $\sqrt{s} = 7$  and 13 TeV and for p-Pb collisions at  $\sqrt{s_{NN}} = 5.02$  TeV follow approximately the same trends. This indicates that, for a given multiplicity,  $K^{*0}$  and  $\phi$  production does not depend on the collision system or energy. The measured  $dN/dy$  values are compared with five different model calculations: PYTHIA6 (Perugia 2011 tune) [15], PYTHIA8 (Monash 2013 tune, both with and without color reconnection) [16], EPOS-LHC [17], and DIPSY [18]. The EPOS-LHC and PYTHIA8 without color reconnection give the best description for the the  $K^{*0}$  while the other PYTHIA calculations exhibit fair agreement with the measured data, and DIPSY overestimates the  $K^{*0}$  yields. The  $\phi$  yields tend to be slightly overestimated

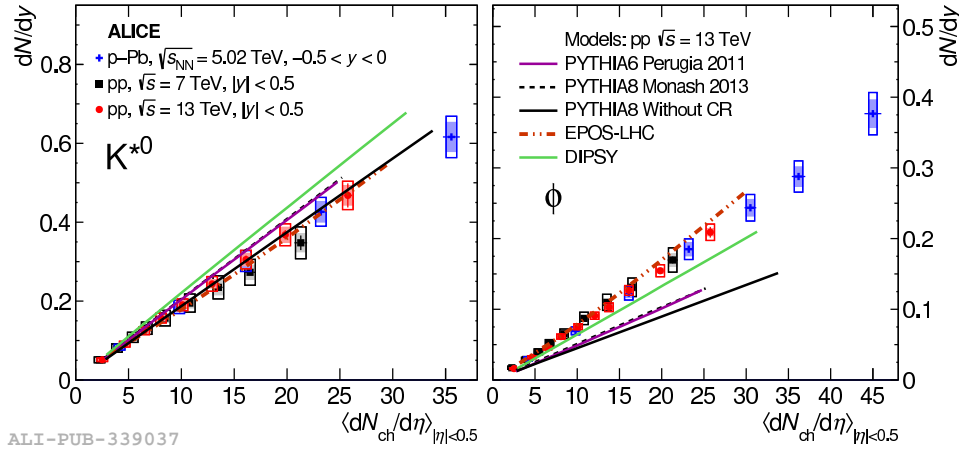


**Figure 2.**  $p_T$ -integrated yields  $dN/dy$  of  $K^{*0}$  (average of the particle and antiparticle) and  $\phi$  as functions of  $\langle dN_{ch}/d\eta \rangle_{|\eta| < 0.5}$ . Results are shown for pp collisions at  $s = 13$  and  $7$  TeV [7, 3], as well as for p-Pb collisions at  $\sqrt{s_{NN}} = 5.02$  TeV [8]. The measurements in pp collisions at  $s = 13$  TeV are also compared with values from common event generators [18, 17, 15, 16]. Bars represent statistical uncertainties, open boxes represent total systematic uncertainties, and shaded boxes show the systematic uncertainties that are uncorrelated between multiplicity classes.

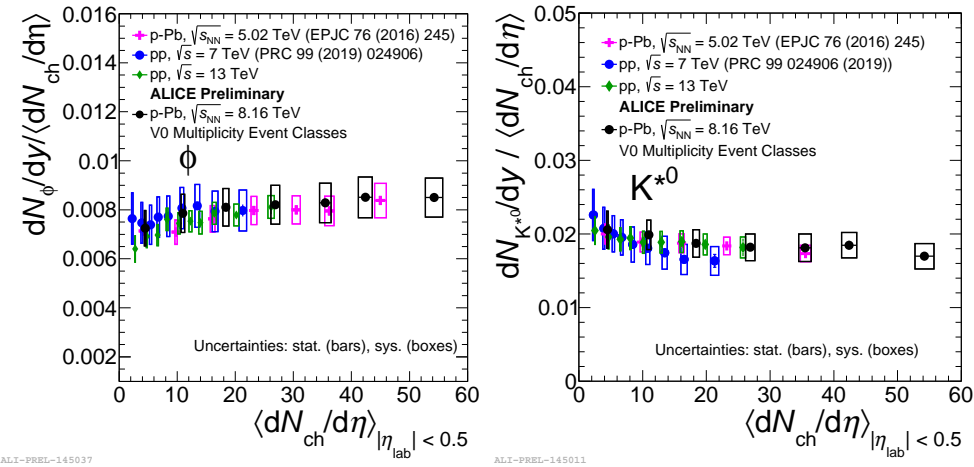


**Figure 3.** Integrated yields of  $K^{*0}$  (left panel) and  $\phi$  (right panel) normalized to  $\langle dN_{ch}/d\eta \rangle_{|\eta_{lab}| < 0.5}$  in pp collisions at  $\sqrt{s} = 7$  and  $13$  TeV and p-Pb collisions at  $\sqrt{s_{NN}} = 5.02$  and  $8.16$  TeV for different multiplicity classes. The bars and the boxes represent the statistical and systematic errors, respectively.

by EPOS-LHC and underestimated by DIPSY and PYTHIA calculations.

The yields normalized to the  $\langle dN_{ch}/d\eta \rangle$  of  $K^{*0}$  and  $\phi$  in pp collisions at  $\sqrt{s} = 7$  and  $13$  TeV, p-Pb collisions at  $\sqrt{s_{NN}} = 5.02$  and  $8.16$  TeV are shown as a function of multiplicity ( $\langle dN_{ch}/d\eta \rangle_{|\eta_{lab}| < 0.5}$ ) in Figure 3. The scaled integrated yield is flat with multiplicity and independent of collision energy and systems for pp and p-Pb collisions within the uncertainties. This confirms that the particle production is mainly driven by charged particle multiplicity irrespectively of collision systems and energies for pp and p-Pb collisions.

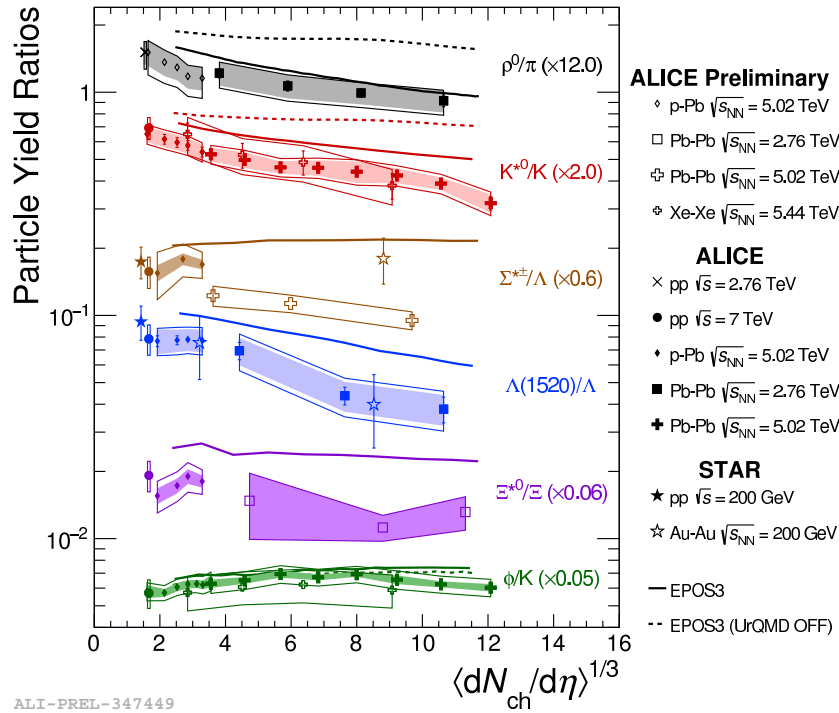


**Figure 4.** Ratios of resonance and stable counterpart yields are reported as a function of multiplicity for the hadronic resonances,  $\rho^0/\pi$ ,  $K^{*0}/K$ ,  $\Sigma^{*\pm}/\Lambda$ ,  $\Lambda(1520)/\Lambda$ ,  $\Xi^{*0}/\Xi$  and  $\phi/K$  from inelastic pp, p–Pb, Pb–Pb and Xe–Xe collisions. The error bars show the statistical uncertainty, while the empty and dark-shaded boxes show the total systematic uncertainty and the uncorrelated contribution across multiplicity bins, respectively. A comparison is also shown to the ratio predicted by the EPOS3 model for Pb–Pb at  $\sqrt{s_{NN}} = 2.76$  TeV, where the late hadronic cascade is simulated with UrQMD. STAR data are also shown for the  $\Sigma^{*\pm}/\Lambda$  and  $\Lambda(1520)/\Lambda$  ratios.

The ratios of  $p_T$ -integrated yields as a function of multiplicity are shown in Figure 4 for pp, p–Pb, Pb–Pb and Xe–Xe collisions, for  $\rho^0/\pi$ ,  $K^{*0}/K$ ,  $\Sigma^{*\pm}/\Lambda$ ,  $\Lambda(1520)/\Lambda$ ,  $\Xi^{*0}/\Xi$  and  $\phi/K$ . Short-lived resonances show a sizable dependence on the multiplicity. A clear suppression is observed for  $\rho^0/\pi$  going from pp to Pb–Pb collisions at  $\sqrt{s_{NN}} = 2.76$  TeV [9]. The EPOS3 event generator [10], which includes UrQMD [11] for the late stage hadronic cascade is able to describe the evolution with multiplicity. The same behavior is observed in the  $K^{*0}/K$  ratio, where the suppression can be observed in a wider multiplicity range with data from pp at  $\sqrt{s} = 7$  TeV, Pb–Pb at  $\sqrt{s_{NN}} = 5.02$  TeV and Xe–Xe at  $\sqrt{s_{NN}} = 5.44$  TeV.

The ratios of  $\Sigma^{*\pm}/\Lambda$  and  $\Lambda(1520)/\Lambda$  show flat behavior in small systems from pp and p–Pb collisions, and the results in Pb–Pb collisions show that  $\Sigma^{*\pm}$  and  $\Lambda(1520)$  are suppressed with respect to the  $\Lambda$  production [13]. Finally, there is no significant centrality dependence of the  $\Xi^{*0}/\Xi$  and  $\phi/K$  ratios with multiplicity for all measured systems. This is expected in the context of re-scattering, considering that the  $\Xi^{*0}$  baryon and the  $\phi$  meson live longer than the expected fireball lifetime and therefore their decay daughters will not undergo re-scattering.

Further, to quantify the  $p_T$ -dependence of the rescattering effect observed in Pb–Pb collisions,  $p_T$ -differential yield ratios were studied as shown in Figure 5 [14]. At low  $p_T$ , the  $K^{*0}/K$  ratio for central collisions is lower than in peripheral (pp) collisions whereas the  $\phi/K$  ratio is comparable within the uncertainties. This observation is consistent with the suppression of  $K^{*0}$  yields due

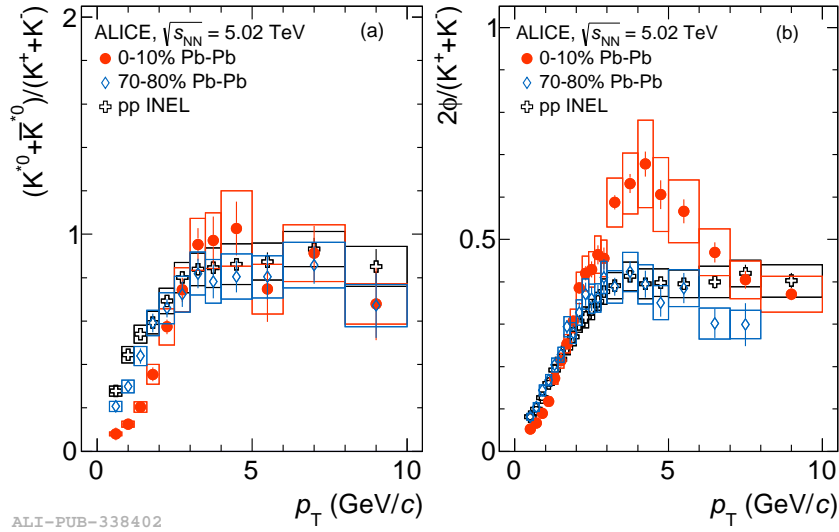


**Figure 5.** Particle yield ratios  $(K^{*0} + \bar{K}^{*0})/(K^+ + K^-)$  in panel (a) and  $(2\phi)/(K^+ + K^-)$  in panel (b), both as a function of  $p_T$  for centrality classes 0-10% and 70-80% in Pb–Pb collisions at  $\sqrt{s_{NN}} = 5.02$  TeV [14]. For comparison, the corresponding ratios are also shown for inelastic pp collisions at  $\sqrt{s} = 5.02$  TeV. The statistical uncertainties are shown as bars and systematic uncertainties are shown as boxes.

to rescattering in the hadronic phase. It indicates that the rescattering affects low momentum particles. At intermediate  $p_T$ , both ratios show enhancement for central Pb–Pb collisions with respect to peripheral and pp collisions. This is in agreement with the presence of a larger radial flow in central Pb–Pb collisions relative to peripheral and pp collisions. For  $p_T > 6$  GeV/c, the  $K^{*0}/K$  and  $\phi/K$  yield ratios in central collisions are similar to peripheral and pp collisions. It demonstrates that fragmentation is the dominant hadron production mechanism in this  $p_T$  region.

### 3.3. Mean transverse momentum

The mean transverse momentum ( $\langle p_T \rangle$ ) values for each multiplicity event class are obtained by integrating the  $p_T$ -spectra in the measured range and by using a fit function to extrapolate the yields in the unmeasured  $p_T$  region. Figure 6 shows the  $\langle p_T \rangle$  of proton,  $K^{*0}$  and  $\phi$  as a function of the average charged particle multiplicity density ( $\langle dN_{ch}/d\eta \rangle$ ) measured at mid-rapidity ( $|\eta| < 0.5$ ) in pp collisions at  $\sqrt{s} = 7$  and 13 TeV and compared with the results obtained in p–Pb at  $\sqrt{s_{NN}} = 5.02$  TeV and Pb–Pb collisions at  $\sqrt{s_{NN}} = 5.02$  and 2.76 TeV.

For all the particles, an increase in  $\langle p_T \rangle$  from low to high multiplicity classes is observed. The same increasing trend of the  $\langle p_T \rangle$  as a function of the multiplicity is observed in pp collisions at  $\sqrt{s} = 7$  TeV and 13 TeV and a mass ordering of  $\langle p_T \rangle$  is found to be followed in central and semi-central Pb–Pb collisions as expected from the hydrodynamic expansion of the system [22]. However, this breaks down for smaller systems. The increase in  $\langle p_T \rangle$  is steeper for smaller systems.

### 3.4. Strangeness production

To understand the strangeness production, the particle yields are measured in various collision systems at different energies. Figure 5 presents yield-ratios of various strange and non-strange hadrons to pions as a function of the mean charged-particle multiplicity  $\langle dN_{ch}/d\eta \rangle_{|\eta| < 0.5}$  for

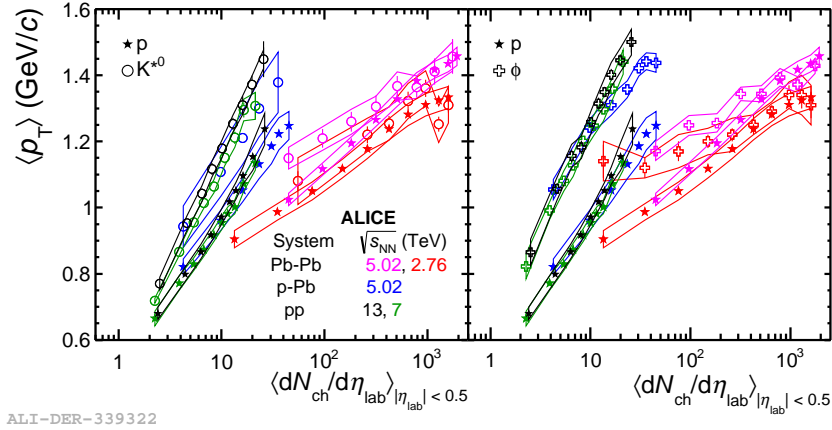


**Figure 6.** Mean transverse momentum ( $\langle p_T \rangle$ ) of  $K^*0$ ,  $\phi$  and  $p$  in pp at  $\sqrt{s} = 7$  and 13 TeV, p-Pb at  $\sqrt{s_{NN}} = 5.02$  TeV and Pb-Pb at  $\sqrt{s_{NN}} = 2.76$  and 5.02 TeV collisions as function of multiplicity. The bars represent the statistical error and the lines represent the systematic error.

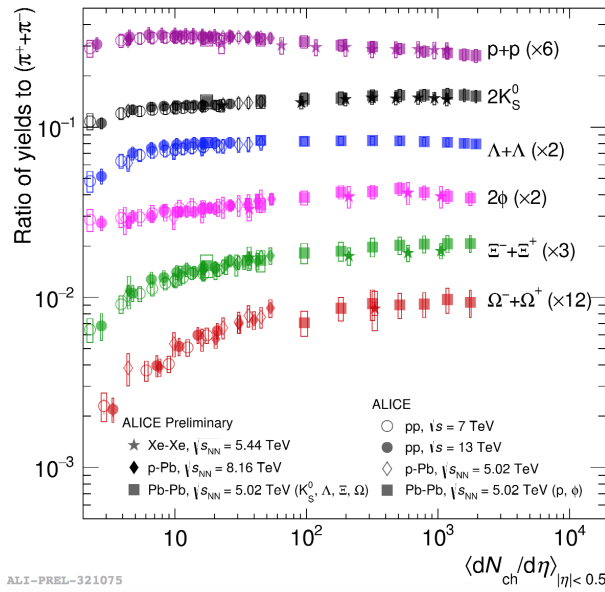


**Figure 7.**  $p/\pi$ ,  $K_s^0/\pi$ ,  $\Lambda/\pi$ ,  $\Xi/\pi$ ,  $\Omega/\pi$  and  $\phi/\pi$  ratios as a function of  $\langle dN_{ch}/d\eta \rangle_{|\eta| < 0.5}$  in different collision systems, pp at  $\sqrt{s} = 7$  [19] and 13 TeV, p-Pb at  $\sqrt{s_{NN}} = 5.02$  TeV [20, 21], Pb-Pb at  $\sqrt{s_{NN}} = 5$  TeV and Xe-Xe at  $\sqrt{s_{NN}} = 5.44$  TeV.

different collision systems and different energies. The ratios of all strange particle yields to pions increase with  $\langle dN_{ch}/d\eta \rangle_{|\eta| < 0.5}$  and saturate in larger collision systems such as Pb-Pb and Xe-Xe collisions. The magnitude of the increase depends on strangeness content. It is observed that the ratios are consistent at similar multiplicities in all collision systems at all LHC energies.

In order to investigate the behavior of hidden strangeness,  $p_T$ -integrated yield ratios of  $\phi$  ( $|S|=0$ ) to  $K$  ( $|S|=1$ ) and  $\Xi$  ( $|S|=2$ ) to  $\phi$  ( $|S|=0$ ) are compared as shown in Figure 8. The  $\phi/K$  ratio shows flat or slightly increasing trend at lower multiplicities that suggests  $\phi$  behaves like a  $S \geq 1$  particle. The ratio of  $\Xi/\phi$  increases with increasing  $\langle dN_{ch}/d\eta_{lab} \rangle_{|\eta| < 0.5}$  for low-multiplicity

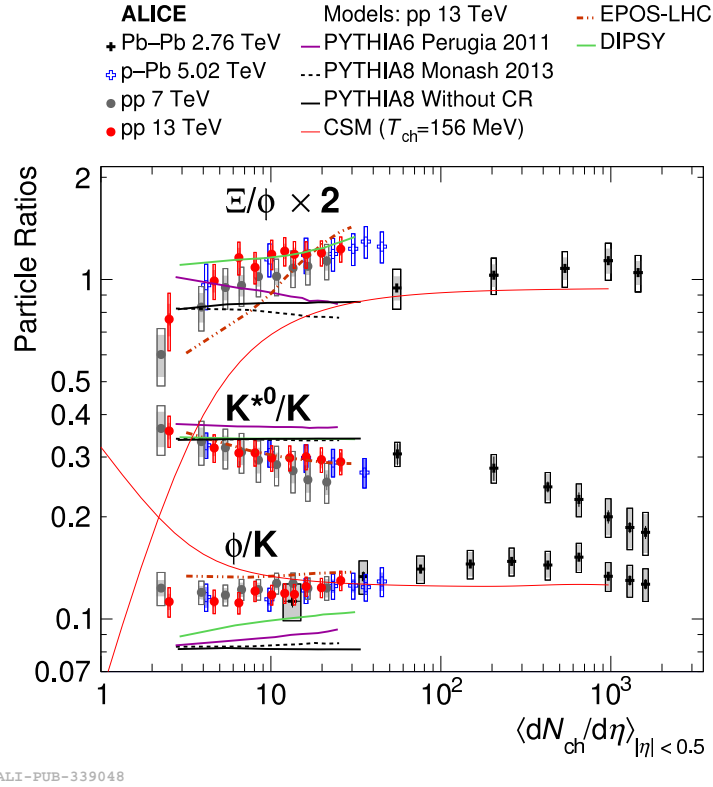


**Figure 8.** Ratios of  $p_T$ -integrated particle yields  $K^{*0}/K$ ,  $\phi/K$ , and  $\Xi/\phi$  in pp collisions at  $\sqrt{s} = 13$  TeV as functions of  $\langle dN_{ch}/d\eta \rangle_{|\eta| < 0.5}$  [24]. These measurements are compared with data from p-Pb collisions at  $\sqrt{s_{NN}} = 5.02$  TeV [9, 10] and Pb-Pb collisions at  $\sqrt{s_{NN}} = 2.76$  TeV [43, 44], as well as results from common event generators [28, 33, 58, 59] and a Canonical Statistical Model calculation [23].

collisions and is then fairly constant for a wide range of multiplicities from high-multiplicity pp and p-Pb collisions to central Pb-Pb collisions. The multiplicity evolution of  $\phi/K$  and  $\Xi/\phi$  ratios suggests that the  $\phi$  has effective strangeness between 1 and 2 units.

### 3.5. Nuclear modification factors

The nuclear modification factor  $R_{AA}$  is used to study medium-induced effects in heavy-ion collisions. The  $R_{AA}$  is the ratio of the yield of a particle in nucleus-nucleus collisions to its yield in pp collisions. This ratio is scaled by the number of binary nucleon-nucleon collisions in each centrality class, which is estimated from Glauber model calculations. For each  $p_T$  bin,

$$R_{AA} = \frac{1}{\langle N_{coll} \rangle} \cdot \frac{dN_{AA}/dp_T}{dN_{pp}/dp_T} \quad (1)$$

The nuclear modification factors measured in 0-10% central Pb-Pb collisions at  $\sqrt{s_{NN}} = 5.02$  TeV for charged pions, charged kaons, (anti)protons,  $K^{*0}$  and  $\phi$  are presented on the left panel in Figure 9. And the  $R_{AA}$  of  $\rho^0$  meson [9] are reported with charged pions, charged kaons, (anti)protons in 0-20% (middle panel) and 60-80% (right panel) in Figure 9. At high transverse momenta ( $p_T > 8$  GeV/c), the production of all hadrons is suppressed by a similar amount and there is no dependence of the suppression on particle mass or quark content within uncertainties.

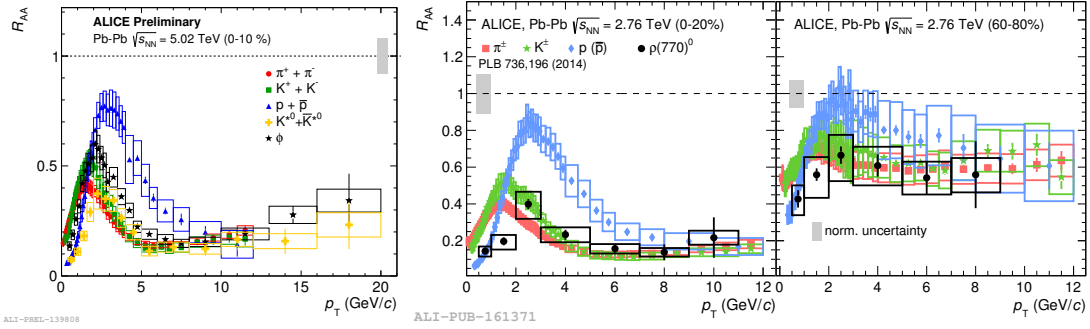


**Figure 9.** Nuclear modification factors  $R_{AA}$  measured for charged pions, charged kaons, (anti)protons and,  $K^{*0}$  and  $\phi$  meson (left panel) in 0-10% Pb-Pb collisions at  $\sqrt{s_{NN}} = 5.02$  TeV. The  $R_{AA}$  of  $\rho^0$  mesons in 0–20% (middle panel) and 60–80% (right panel) central Pb-Pb collisions at  $\sqrt{s_{NN}} = 2.76$  TeV with charged pions, charged kaons, (anti)protons. The statistical and systematic uncertainties are shown as bars and boxes, respectively.

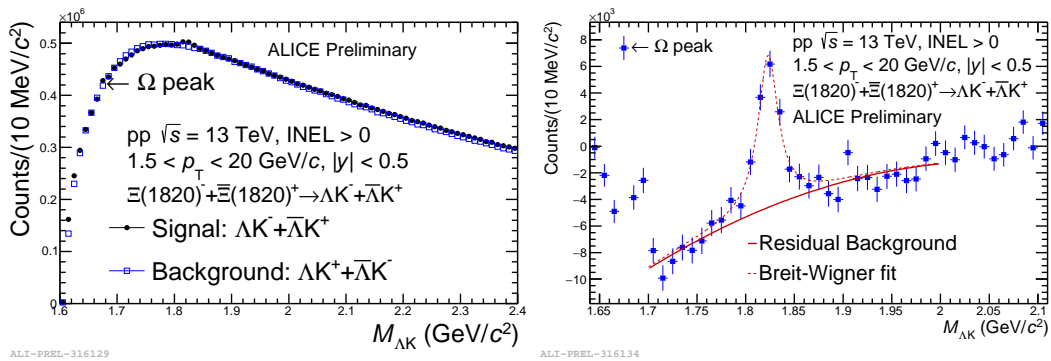


**Figure 10.** (Left) The  $\Lambda K$  Invariant mass distribution in  $p_T$  bins 1.5 – 20 GeV/c and for the INEL > 0 event class. (Right) The invariant mass distribution after subtraction of the background. The dashed curve represents the combined fit, while the solid line describes the residual background.

There is a species dependence of  $R_{AA}$  at intermediate transverse momentum ( $2 < p_T < 8$  GeV/c), which is likely to be a result of an interplay between different effects such as radial flow, low- $p_T$  suppression, species dependent  $p_T$  shapes of the pp reference spectra.

### 3.6. Reconstruction of $\Xi(1820)$

The first measurement of  $\Xi(1820)$  from collider experiments is shown in Figure 10. The calculation from FASTSUM Collaboration [25] shows potential parity doubling of strange resonant states, which could be a signature of chiral symmetry restoration in heavy-ion collisions. The positive-parity masses are largely temperature-independent while negative-parity masses drop and become near-degenerate with the corresponding positive-parity mass close to critical temperature. Because the  $\Xi(1820)$  has negative-parity, the comparison of mass shift, width broadening or change in yield to the positive-parity  $\Xi(1530)$  can be one of the key measurements to study chiral symmetry restoration.

#### 4. Summary

A comprehensive set of resonance and strangeness production measurements in all available collision systems is presented. The  $p_T$ -integrated yields normalized by the average charged particle multiplicity are observed to be constant as a function of charged particle multiplicity. The ratios of  $p_T$ -integrated particle yields for various resonances are measured and  $\rho^0/\pi$ ,  $K^{*0}/K$  and  $\Lambda(1520)/\Lambda$  exhibit a decrease from pp and peripheral Pb–Pb to central Pb–Pb collisions. This behavior can be explained by the dominance of re-scattering of decay daughters over regeneration in the hadronic phase. The increase of  $\langle p_T \rangle$  is observed from low to high multiplicity classes and a mass ordering of  $\langle p_T \rangle$  is found in central Pb–Pb collisions. The  $\phi$  meson with hidden strangeness seems to have an effective strangeness between 1 and 2 units. The nuclear modification factors for resonances are suppressed at high  $p_T$  for Pb–Pb collisions and the amount of suppression is similar to charged pions, charged kaons, (anti)protons. The first measurement of  $\Xi(1820)$  is presented and will be compared to the corresponding positive-parity particle to study chiral symmetry restoration.

#### References

- [1] J. Stachel, A. Andronic, P. Braun-Munzinger, and K. Redlich *J. Phys. Conf. Ser.* **509** (2014) 012019
- [2] S. Acharya *et al.* (ALICE Collaboration), arXiv:1610.03001
- [3] S. Acharya *et al.* (ALICE Collaboration), *Phys. Rev. C* **99** (2019) 024906
- [4] S. Acharya *et al.* (ALICE Collaboration), *Nucl. Phys. A* **971** (2018) 1-20
- [5] K. Aamodt *et al.* (ALICE Collaboration), *Int. J. Mod. Phys* **29** (2014) 1430044
- [6] M. Tanabashi *et al.* (Particle Data Group Collaboration), *Phys. Rev. D* **98** no. 3,(2018) 030001
- [7] S. Acharya *et al.* (ALICE Collaboration), arXiv:1910.14397
- [8] S. Acharya *et al.* (ALICE Collaboration), *Eur. Phys. J. C* **76** (2016) 245
- [9] S. Acharya *et al.* (ALICE Collaboration), *Phys. Rev.* **C99** 064901
- [10] K. Werner, B. Guiot, I. Karpenko, and T. Pierog *Phys. Rev.* **C89** (2016) 064903
- [11] M. Bleicher *et al.* *J. Phys.* **G25** (1999) 1859-1869
- [12] B. I. Abelev *et al.* (STAR Collaboration), *Phys. Rev. Lett.* **97** (2006) 132301
- [13] S. Acharya *et al.* (ALICE Collaboration), *Phys. Rev.* **C99** 024905
- [14] S. Acharya *et al.* (ALICE Collaboration), arXiv:1910.14419
- [15] P. Z. Skands, *Phys. Rev. D* **82** (2010) 074018
- [16] P. Z. Skands, S. Carrazza, and J. Rojo, *Eur. Phys. J. C* **74** (2014) 3024
- [17] T. Pierog *et al.* *Phys. Rev. C* **92** (2016) 034906
- [18] C. Flensburg, G. Gustafson, and L. Lönnblad, *J. High Energy Phys.***8** (2011) 103
- [19] J. Adam *et al.* (ALICE Collaboration) *Nat. Phys.* **13** 535-539 (2017)
- [20] J. Adam *et al.* (ALICE Collaboration) *Phys. Lett. B* **728** (2014) 25-38
- [21] J. Adam *et al.* (ALICE Collaboration) *Phys. Lett. B* **758** (2016) 389-401
- [22] C. Shen, U. Heinz, P. Houvinen, and H. Song *Phys. Rev.***C84** (2011) 044903
- [23] S. Acharya *et al.* (ALICE Collaboration), *Phys. Rev. C* **99** (2019) 024906
- [24] S. Acharya *et al.* (ALICE Collaboration), arXiv:1908.01861
- [25] G. Aarts, C. Allton, D. Boni, S. Hands, B. Jäger, C. Praki, and J.I. Skullerud. *EPJ Web Conf.* **171** (2018) 14005